PHYSICAL REVIEW A **68**, 023406 (2003)

Direct imaging of rotational wave-packet dynamics of diatomic molecules

P. W. Dooley,[1,2] I. V. Litvinyuk,[1] Kevin F. Lee,[1,2] D. M. Rayner,[1] M. Spanner,[1,3] D. M. Villeneuve,[1] and P. B. Corkum[1,2]
[1]*Steacie Institute for Molecular Sciences, National Research Council of Canada, 100 Sussex Drive, Ottawa, Ontario, Canada K1A 0R6*
[2]*Department of Physics & Astronomy, McMaster University, 1280 Main Street West, Hamilton, Ontario, Canada K1S 5P3*
[3]*Department of Physics, University of Waterloo, Waterloo, Ontario, Canada N2L 3G1*

(Received 11 April 2003; published 25 August 2003)

We use linearly polarized 45 fs pulses to create rotational wave packets in N_2 and O_2. We Coulomb explode molecules with a high-intensity circularly polarized pulse and use an ion imaging detector to measure a series of two-dimensional projections of the wave packet's angular distribution in 27 fs increments. We highlight the evolving wave packet near the first, second, sixth, and tenth full revival times and also near the one-eighth, one-quarter, one-half, and three-quarter fractional revivals.

DOI: 10.1103/PhysRevA.68.023406 PACS number(s): 33.80.Rv, 33.80.Gj

I. INTRODUCTION

The translational and rotational behavior of gas phase molecules can be controlled using the large Stark shifts produced by intense laser pulses [1]. Such pulses have been used to trap [2], focus [3], and spin molecules [4]. The ability of intense laser pulses to produce rotational wave packets [5–8] that exhibit transient molecular alignment is of particular interest. Aligned molecules are advantageous for applications such as surface scattering research [9], surface catalysis [10], and surface processing [11].

Strong field alignment requires an anisotropic polarizability leading to different Stark shifts along at least two molecular axes. If the laser field is applied adiabatically, the molecule aligns with its most polarizable axis along the laser polarization direction [5–8]. If the pulse duration is short relative to the molecular rotational period, the molecule experiences an impulse toward alignment [12,13]. In that case, the resulting rotational wave packet exhibits transient alignment after the pulse is over. For linear molecules, the alignment is reproduced in a series of full revivals at intervals of one fundamental rotational period. Rotational wave packets can also be produced by rapidly truncating an adiabatic aligning pulse [14].

Many applications benefit from molecular alignment [9–11,15,16]. The presence of a strong aligning laser field is not a perturbation, however, and can interfere with subsequent measurements. Therefore, transient alignment has the advantage of producing field-free aligned molecules for short pulse experiments [12].

To extract quantitative information in the molecular frame from measurements made in the laboratory frame, the complete angular distribution function must be known. There are two approaches to obtaining the angular distribution function. (1) The amplitude and phase of all rotational states that are thermally or nonthermally populated must be measured. This could be achieved by Fourier transforming a single time-dependent parameter characteristic of the wave packet's dynamics and comparing the result to a numerical simulation for similar aligning pulse parameters [13]. (2) The distribution function can be measured directly at a particular time. In this paper, we demonstrate the latter approach and illustrate the equivalence of the two methods.

In our experiments, a 45 fs linearly polarized "aligning" pulse creates a wave packet that exhibits macroscopic field-free molecular alignment at well-defined time delays. We observe the time evolution of the wave packet using an intense, circularly polarized "exploding" pulse. At each time delay, molecules are multiply ionized by the exploding pulse and undergo rapid dissociation (Coulomb explosion). The resultant atomic ion fragments are analyzed to yield the three-dimensional velocity of each immediately following the Coulomb explosion. For a diatomic molecule, such initial velocities are parallel to the molecular axis if the dissociation is rapid. Hence, we directly measured the distribution of molecular orientations for the rotational wave packet at various points during its time evolution.

We use a circularly polarized exploding pulse and consider only angles within the plane of polarization. This is important because Coulomb explosion is most efficient for molecules oriented parallel to the laser polarization [17]. With circular polarization, the ionization probability depends solely upon the out-of-plane angle [18]. Since the in-plane angle is unbiased, our measured angular distributions accurately reflect the actual molecular ensemble.

Our work is presented as follows. Our general experimental approach is described in the following section. Experiments conducted to characterize the Coulomb explosion of N_2 and to select N^{3+} ions originating from the $N_2^{5+} \rightarrow N^{2+} + N^{3+}$ dissociation channel are described in Sec. II. In Sec. III, revival structures of N_2 rotational wave packets (derived from the measured N^{3+} angular distributions) are presented, modeled, and compared with O_2 revival structures. The effects of centrifugal deformation, nuclear spin, and aligning pulse intensity on the revival structures are discussed. In Sec. IV, we present measured angular distributions corresponding to full and fractional rotational revivals in N_2 and O_2. Of particular interest is the 1/8 revival in O_2 that occurs in a featureless region of the alignment revival structure. Our time-dependent angular distributions are depicted as polar representations, intensity maps, and projections onto basis states.

II. EXPERIMENTAL CONFIGURATION

The laser system consisted of a Ti:sapphire oscillator and regenerative amplifier and produced linearly polarized, 800 μJ, 800 nm wavelength pulses at a repetition rate of 500 Hz. The pulse duration after the regenerative amplifier was measured to be 39 fs using SPIDER [19] and estimated to be 45 fs in the experimental chamber. A Mach-Zehnder interferometer was used to divide the laser output into aligning and exploding pulses, to introduce a relative time delay, and to recombine the two beams collinearly. A telescope was installed in the aligning pulse arm of the interferometer to decrease the beam diameter by a factor of 2. This produced an aligning focus whose minimum cross-sectional area and confocal parameter were each four times greater than those of the exploding pulse and ensured that only those molecules upon which the aligning pulse had acted most strongly were exploded. A quarter wave plate was used to circularly polarize the exploding pulse. The interferometer's beam combiner was used at near-normal incidence to preserve the polarization states of the two pulses. The 10 μJ aligning and 200 μJ exploding pulses entered an ultrahigh-vacuum experimental chamber and were focused by an on-axis parabolic mirror ($f/2$, $f = 50$ mm) into a well-collimated beam of nitrogen molecules.

The experimental chamber consisted of three differentially pumped sections separated by two 1 mm diameter skimmers. Operating pressures in the source, intermediate, and explosion subchambers were 7×10^{-5} mbar, 1×10^{-8} mbar, and 2×10^{-9} mbar, respectively. A molecular jet was produced by expanding 33 mbar of N_2 through a circular aperture (100 μm diameter) into the source chamber. Collimation of the jet was achieved using the two skimmers and a piezoelectric slit mounted in the explosion chamber. Beyond the slit, the cross section of the molecular beam was rectangular ($1.5\ \mathrm{mm}\times40\ \mu\mathrm{m}$). The laser propagation direction was along the thin (40 μm) dimension of the molecular beam. Geometric constraints limited the molecular beam's transverse translational temperature to <0.01 K. The measured longitudinal temperature was 90 K.

Since the molecular beam thickness was approximately equal to the aligning focus' confocal parameter, target molecules were confined to the high-intensity region of the aligning focal volume. The number density of the molecular beam was $\sim10^{10}$ molecules/cm^3 beyond the slit, corresponding to ~10 molecules within the overlap region of the aligning laser and molecular beams. While the interaction volumes of the two foci were approximately equal, the confocal parameter of the exploding focus was a factor of 4 smaller than that of the aligning focus. As a result, less than one molecule per laser pulse was present in the high-intensity region of the exploding focus, i.e., the region in which the most highly charged Coulomb explosion channels were active. By selecting a high-charge Coulomb explosion channel, we probed only those molecules located at the center of the aligning focal volume.

A uniform acceleration time-of-flight mass spectrometer (100 V/cm, 240 mm ion flight length, 70 mm internal diameter) was used for ion collection and analysis. The mass spectrometer axis, molecular beam, and laser beams were mutually orthogonal. Ion impact data were recorded using a helical delay line imaging detector (Roentdek DLD-80) [20] in conjunction with five current preamplifiers, five constant-fraction discriminators, and a multiple hit time-to-digital converter (LeCroy TDC3377). Using this data acquisition system, the ion arrival time and two-dimensional impact position were recorded for up to 16 ions per laser pulse. The ion impact data were used to determine the initial, three-dimensional velocity vector for each Coulomb explosion fragment and hence the orientation of the exploded molecule.

III. COULOMB EXPLOSION DIAGNOSTIC EXPERIMENTS

To perform accurate imaging of rotational wave packets using our technique, an appropriate Coulomb explosion channel must be selected. Strong field ionization of N_2 using our 4×10^{15} W/cm^2 exploding pulse produced parent ions ranging from ${N_2}^{+}$ to ${N_2}^{6+}$. Dissociation of the parent ions produced fragments ranging from N^{+} to N^{3+} [Fig. 1(a)]. The six active fragmentation channels can be identified from a correlation map analogous to that discussed by Frasinski *et al.* [21] [Fig. 1(b)]. For accurate imaging, a high-charge dissociation channel must be selected to ensure that the molecule dissociates before molecular reorientation can occur. This criterion ensures that the momenta of fragment ions are parallel to the molecular axis. For our exploding pulse, the two most highly charged Coulomb explosion channels were ${N_2}^{5+}\rightarrow N^{2+}+N^{3+}$ and ${N_2}^{6+}\rightarrow N^{3+}+N^{3+}$ [boxes 5 and 6 in Fig. 1(b), respectively].

The limitations of our detection electronics also influenced our choice of Coulomb explosion channel. The pulse pair resolution of each of our five constant-fraction discriminators is ~15 ns. As a result, certain molecular orientations are detected less efficiently for explosion channels that produce identical fragments (such as ${N_2}^{6+}\rightarrow N^{3+}+N^{3+}$). This nonuniform detection efficiency for symmetric dissociation channels gives rise to the unshaded "dead zone" which runs diagonally through boxes 1, 4, and 6 in Fig. 1(b). All molecular orientations are (in principle) equally detectable for asymmetric channels, however [as evidenced by the continuous dark streaks in boxes 2 and 5 in Fig. 1(b)]. Therefore, our wave-packet imaging was performed using only fragments originating from the asymmetric ${N_2}^{5+}\rightarrow N^{2+}+N^{3+}$ channel.

Conservation of momentum was used to select N^{2+} and N^{3+} fragments originating from the desired ${N_2}^{5+}\rightarrow N^{2+}+N^{3+}$ dissociation channel. The total N^{2+} and N^{3+} yields [Figs. 2(a) and 2(b)] are composed of overlapping contributions from various explosion channels. To identify fragments produced via the desired channel, we rely on the fact that the vector sum of a N^{2+} fragment's momentum ($\mathbf{p}_{2+}$) and a N^{3+} fragment's momentum ($\mathbf{p}_{3+}$) is zero if they originate from the same ${N_2}^{5+}$ parent ion. We imposed this constraint experimentally by summing the momenta of each possible $N^{2+}-N^{3+}$ pair recorded for each laser pulse [Fig. 2(c)]. Only those fragment pairs that satisfied the condition $\mathbf{p}_{2+}+\mathbf{p}_{3+}<15$ atomic units [i.e., the gray areas in Figs. 2(a) and

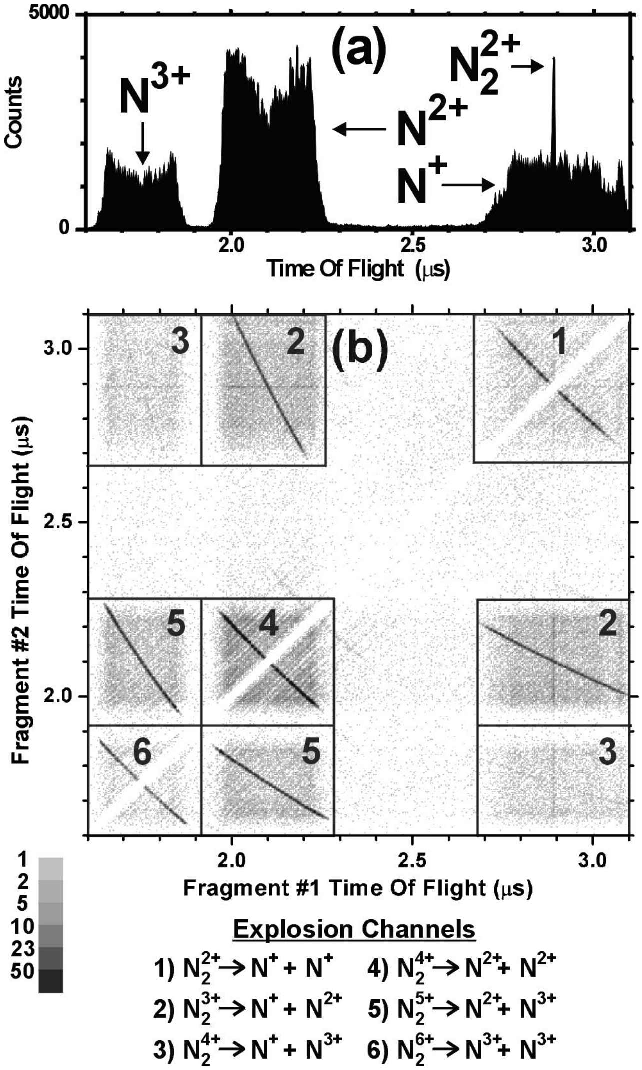

FIG. 1. (a) Nitrogen fragment time-of-flight spectrum. Coulomb explosion of N_2 using our exploding pulse produces N^+, N^{2+}, and N^{3+} fragments via numerous dissociation channels. Some unexploded $N_2{}^{2+}$ is also observed. (b) N_2 Coulomb explosion correlation map. For each exploding pulse, the individual detector impact times of all possible nitrogen fragment pairs are plotted against each other. Each numbered box contains fragment pair data for a specific dissociation channel (see legend). Within each box, the dark diagonal (top left to bottom right) streak results from correlated fragment pairs, i.e., fragments originating from the same N_2 molecule. The diffuse shading within each box stems from false coincidences. The narrow unshaded region (diagonal from bottom left to top right) arises from the 16 ns pulse pair resolution of the constant fraction discriminator used for fragment impact timing.

2(b)] were considered to have originated from the desired channel and retained. The imposition of this constraint clearly shows that the $N_2{}^{5+} \rightarrow N^{2+} + N^{3+}$ channel is characterized by fragment kinetic energies in the 15–25 eV range [Figs. 2(a) and 2(b)].

IV. WAVE-PACKET REVIVAL STRUCTURES

The time evolution of the wave packet produced by the aligning pulse can be written as a sum over the molecular rotational states:

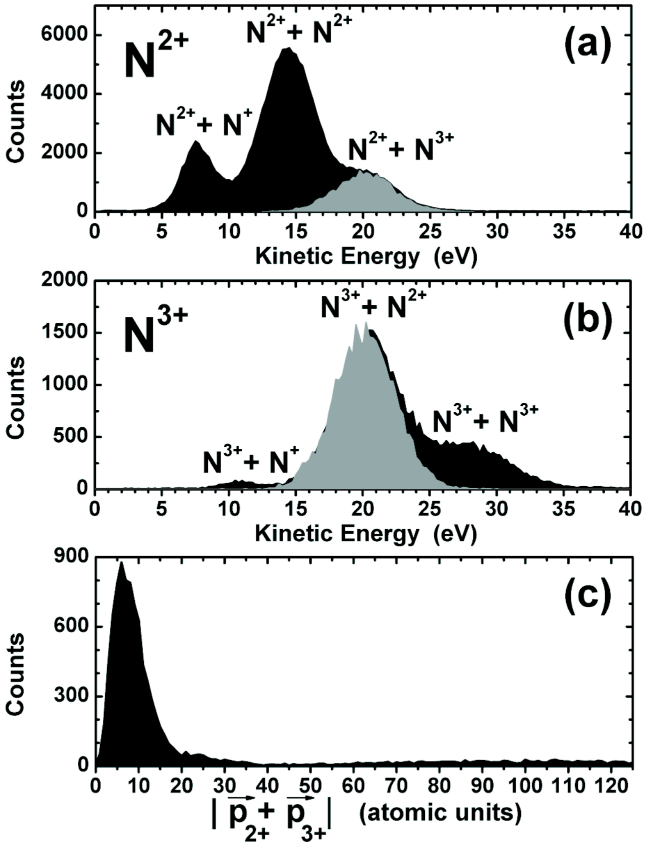

FIG. 2. Selection of $N_2{}^{5+} \rightarrow N^{2+} + N^{3+}$ channel. The kinetic energy spectra for N^{2+} and N^{3+} fragments consist of overlapping contributions from various Coulomb explosion channels [black regions in panels (a) and (b), respectively]. Panel (c) is a histogram of the three-dimensional momentum sum for all N^{2+}-N^{3+} fragment pairs. The desired $N_2{}^{5+} \rightarrow N^{2+} + N^{3+}$ channel was selected by retaining only low (<15 atomic units) total momentum pairs and exhibits a characteristic 15–25 eV fragment energy [gray regions in panels (a) and (b)].

$$\Psi(t) = \sum_J a_J e^{-i(E_J/\hbar)t} |J,M\rangle, \tag{1}$$

where E_J are the energy eigenvalues, $|J,M\rangle$ are spherical harmonics, and M are with respect to the polarization axis of the aligning pulse. Note that the cylindrical symmetry of the optical potential prevents the coupling of different M values. For convenience, we omit the M dependence of the kets in the following discussion. For the lowest vibrational state of the molecule $(v=0)$, the rotational energies are given by $E_J \approx hcB_0 J(J+1)$, where h is Planck's constant, c is the speed of light in vacuum, and B_0 is the ground state rotational constant. For wave packets containing high-$|J\rangle$ states, centrifugal distortion of the molecule must be taken into account. In such cases, the energy eigenvalues become

$$E_J = hc[B_0 J(J+1) + D_e J^2 (J+1)^2], \tag{2}$$

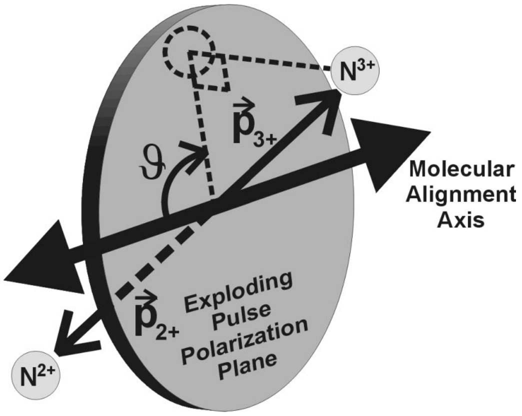

FIG. 3. Definition of observation angle ϑ. Since $N_2^{5+} \rightarrow N^{2+} + N^{3+}$ is a prompt dissociation channel, the momentum of each fragment is parallel to the molecular axis. Thus, a single fragment momentum measurement is sufficient to determine a molecule's orientation. The three-dimensional momentum of each N^{3+} fragment was projected onto the polarization plane of the exploding pulse. The angle ϑ between the momentum projection and the molecular alignment (i.e., aligning pulse polarization) axis was then measured.

where D_e is the deformation constant for the nonvibrating molecule [22]. For N_2, $B_0 = 1.989\,581$ cm^{-1} and $D_e = 5.76 \times 10^{-6}$ cm^{-1} [23].

We observed the field-free evolution of the rotational wave packet created by the aligning pulse by Coulomb exploding N_2 at successive time delays (27 fs increments). The peak intensity of the aligning pulse (1.4×10^{14} W/cm^2) was chosen to achieve alignment without ionizing N_2. At each delay, 2000 N^{3+} fragments originating from the $N_2^{5+} \rightarrow N^{2+} + N^{3+}$ dissociation channel (i.e., those with kinetic energies in the 15–25 eV range) were collected. The three-dimensional initial velocity vector for each N^{3+} fragment (which was collinear with the preexplosion orientation of the parent molecule) was then calculated.

The molecular alignment axis (i.e., the polarization axis of the linearly polarized aligning pulse) lay in the polarization plane of the circularly polarized exploding pulse (Fig. 3). We measured the angle ϑ between the alignment axis and the projection of each three-dimensional fragment velocity onto the polarization plane. Since the exploding pulse was circularly polarized, the Coulomb explosion probability was independent of the angle ϑ. Hence, experimental ϑ distributions are unbiased and depend solely upon the actual ensemble of molecular orientations.

Raw ϑ distributions were normalized using a ''background'' ϑ distribution to ensure that a slightly elliptical ($\varepsilon = 0.97$) exploding pulse polarization did not bias the determination of molecular orientations. The background ϑ distribution was obtained in a single pulse experiment by exploding an isotropic ensemble of molecules.

While we measure complete time-dependent ϑ distributions, it is typical (in the revival literature) to plot the first moment of such distributions ($\langle \cos^2 \vartheta \rangle$ in our case) as a function of time. The measured ϑ distributions are presented and discussed in Sec. V. In keeping with convention, we characterized the degree of alignment at each aligning-exploding delay by calculating $\langle \cos^2 \vartheta \rangle$ for each normalized ϑ distribution. In our scheme, $\langle \cos^2 \vartheta \rangle = 0.5$ reflects an isotropic distribution of molecular orientations while $\langle \cos^2 \vartheta \rangle = 1$ indicates complete alignment. The limiting case in which all molecules are perpendicular to the alignment axis is denoted by $\langle \cos^2 \vartheta \rangle = 0$. Note that our measured projection angle ϑ differs from the azimuthal angle of a spherical coordinate system θ (for which $\langle \cos^2 \theta \rangle = 1/3$ reflects an isotropic distribution).

The time evolution of the N_2 alignment parameter $\langle \cos^2 \vartheta \rangle$ is depicted in Fig. 4(a). Prior to the arrival of the aligning pulse (i.e., $t < 0$), the molecular ensemble is isotropic (i.e. $\langle \cos^2 \vartheta \rangle = 0.50$). The arrival of the aligning pulse is followed by a prompt net alignment ($t = T_0 = 0.067$ ps). Neglecting centrifugal distortion, each $|J\rangle$ state within the rotational wave packet accumulates phase with a different angular frequency given by

$$\omega_J = \frac{1}{2} J(J+1)\omega_1, \tag{3}$$

where $\omega_1 = 4\pi B_0 c$ is the fundamental phase frequency, i.e., that of $|1\rangle$. Thus, the constituent $|J\rangle$ states rapidly dephase with respect to each other and the initial net alignment quickly dissipates. The baseline for $t > 0$ is higher than the isotropic value $\langle \cos^2 \vartheta \rangle = 0.5$, however. Known hereafter as ''incoherent alignment,'' this baseline shift is due to the first term in Eq. (A6) and can be understood as follows. Initially (i.e., $t < 0$), the relative $|J\rangle$ state populations were given by a thermal Boltzmann distribution and M values were uniformly populated for each $|J\rangle$ state. The aligning pulse modifies the $|J\rangle$ state distribution by inducing various rotational excitations and deexcitations via Raman transitions. Since there exists a lower bound for Raman deexcitation (i.e., $|0\rangle$) but no such limit for excitation, the resulting wave packet exhibits net rotational excitation, i.e., $\langle J \rangle_{\text{packet}} > \langle J \rangle_{\text{thermal}}$. The laser-molecule interaction does not alter the distribution of M values, however. Thus, rather than being uniformly distributed, the angular momentum vectors of each $|J\rangle$ state in the wave packet are preferentially oriented perpendicular to the aligning pulse polarization. In terms of molecular orientation, this corresponds to a small but persistent net alignment of the ensemble and an elevated experimental baseline (i.e., $\langle \cos^2 \vartheta \rangle > 0.50$) for $t > 0$.

Since the wave packet evolves in a field-free environment, the $|J\rangle$ states eventually begin to rephase. When the accumulated phases of each $|J\rangle$ state are equal (to within multiples of 2π), the initial net alignment is reproduced in an event known as a full wave-packet revival. Since $J(J+1)$ is even for all J, all angular frequencies ω_J are integer multiples of the fundamental frequency ω_1 [Eq. (3)]. Therefore, the time of the first full revival, $t = T_0 + T_1$, is determined by ω_1 according to $T_1 = 2\pi/\omega_1 = (2B_0 c)^{-1} = 8.383$ ps. The net alignment associated with the first full revival ($t = T_0 + T_1 = 8.462$ ps) maximizes 8.395 ps after the initial alignment at time T_0 [Fig. 4(a)]. Since the time increment in the experiment was 27 fs, the result is in agreement with expectation.

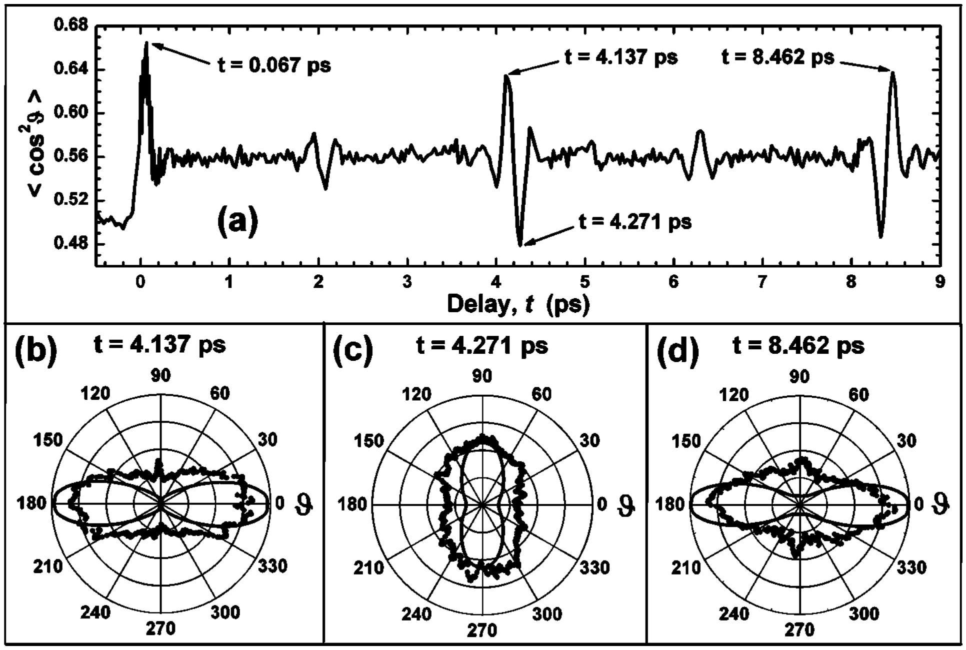

FIG. 4. (a) $\langle\cos^2\vartheta\rangle$ revival structure for N_2. The variation of $\langle\cos^2\vartheta\rangle$ with aligning pulse-exploding pulse delay is depicted. Prior to wave-packet creation $(t<0)$, the molecular ensemble is isotropic and $\langle\cos^2\vartheta\rangle=0.50$. The aligning pulse creates a rotational wave packet at $t=0$ which exhibits maximum field-free alignment at $t=0.067$ ps. Thereafter, an elevated baseline ($\langle\cos^2\vartheta\rangle\sim0.56$) due to incoherent alignment was observed. Significant net alignment and antialignment are observed during the first revival ($t=8.462$ ps) and half revival ($t=4.271$ ps) of the wave packet, respectively. (b)–(d) Plots of measured (dots) and simulated (lines) N_2 ϑ distributions. The molecular alignment axis lies along $\vartheta=0°$ and $\vartheta=180°$ and is therefore horizontal in each figure. The rotational wave packet exhibits significant net alignment prior to the half revival [$t=4.137$ ps; panel (b)] and during the first revival [panel (d)]. Net antialignment is observed during the half revival [panel (c)]. For clarity, the areas of the simulated plots are two-thirds those of the measured distributions.

Significant net alignment and "antialignment" also occur near fractional revival times $t=T_0+T_\eta$, where $T_\eta=\eta T_1$ for $\eta=\frac{1}{4},\frac{1}{2},\frac{3}{4}$. During the η revival, the accumulated phases of states $|J\rangle$ and $|J+2\rangle$ differ by $2\pi\eta$ modulo 2π. For $\eta=\frac{1}{2}$, the relative phases of all $|J\rangle$ states differ by integer multiples of π. At the half revival, the sets of even $|J\rangle$ states corresponding to $J=0,4,8,\ldots$ and odd $|J\rangle$ states given by $J=3,7,11,\ldots$ are precisely in phase with each other. However, they are π out of phase with the set consisting of $J=2,6,10,\ldots$ and $J=1,5,9,\ldots$. The net result is destructive interference along the alignment axis and a localization of the wave packet in the plane perpendicular to it. Hence, significant net antialignment is expected at the first half-revival time $t=T_0+T_1/2=4.259$ ps. In fact, the minimum value of $\langle\cos^2\vartheta\rangle$ occurred at $t=4.271$ ps [Fig. 4(a)], in excellent agreement with the predicted half-revival time.

Full revivals of the wave packet occur at integer multiples of the first revival time, i.e., $t=T_0+T_n$, where $T_n=nT_1$ for $n=1,2,3,\ldots$. The time evolution of the N_2 alignment parameter for the first, second, sixth, and tenth full wave-packet revivals ($n=1,2,6,10$) is depicted in Figs. 5(a)–5(d), respectively. The measured (predicted) times of maximum net alignment for each revival were $t=8.462$ ps (8.450 ps), 16.857 ps (16.832 ps), 50.476 ps (50.364 ps), and 83.990 ps (83.895 ps). Each full revival occurred slightly later than predicted. The time lag results from a perturbation of the angular frequencies ω_J due to centrifugal distortion that was neglected in Eq. (3). Note that the time evolution of the alignment parameter $\langle\cos^2\vartheta\rangle$ is not identically reproduced for each revival. While the $n=1$ data [Fig. 5(a)] exhibit inversion symmetry about $t\sim8.4$ ps, the modulation structure becomes increasingly asymmetric, i.e., "chirped," for each successive revival. The observed chirp is a further consequence of the additional nonlinearity introduced into the ω_J frequency spectrum by centrifugal distortion.

The rotational wave packet's creation by the aligning pulse and its subsequent time evolution were numerically simulated (see the Appendix for details). Results for a 48.4 fs full width at half maximum $\sin^2$ pulse of peak intensity $1.7\times10^{14}\mathrm{W/cm^2}$ are depicted in Fig. 5. An initial rotational temperature of 105 K was assumed. The model quite successfully predicts the times corresponding to maximum net alignment as well as the chirp of the revival structure. Unlike the model, the baseline of the experimental data decreases gradually toward an isotropic value of $\langle\cos^2\vartheta\rangle=0.5$ with each successive revival. The decay is not due to molecular collisions since the mean collision time is ~0.1 s, nor is it a result of molecules entering and leaving the laser foci since molecules travel less than 0.1 μm during the measurement. The observed decay is most likely an artifact due to a slight relative shift of the exploding pulse focus with aligning-exploding delay. In such a case, the overlap between aligning and exploding foci would degrade with increasing delay and consequently the exploded molecules would exhibit decreasing incoherent alignment.

The Fourier transform of the time-dependent alignment

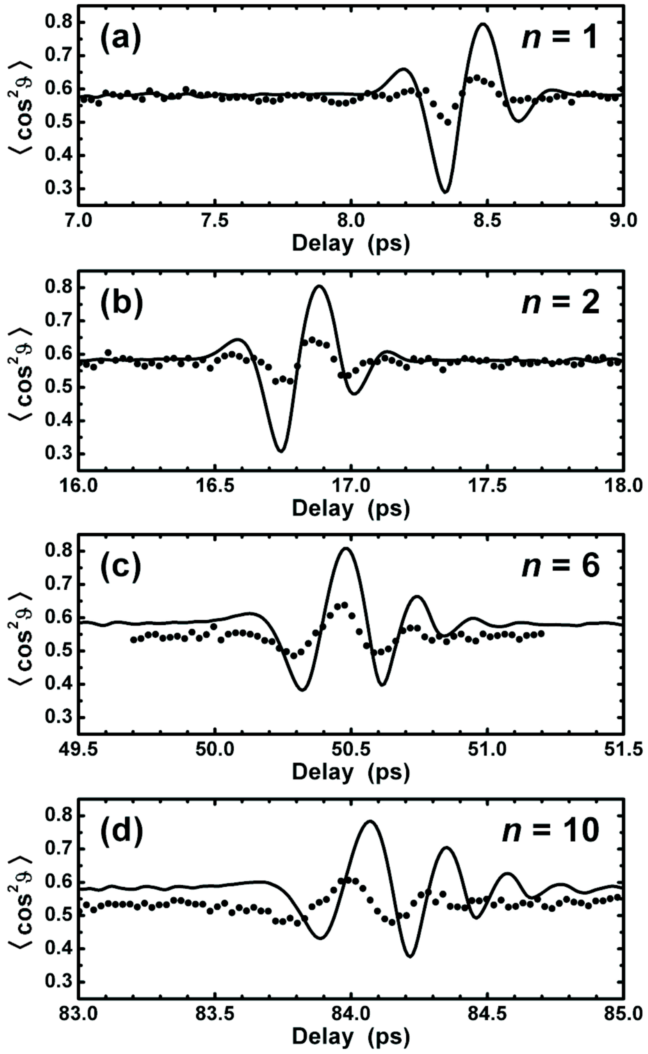

FIG. 5. Selected full revivals for N_2. The measured time dependence of $\langle\cos^2\vartheta\rangle$ (dots) for the (a) first, (b) second, (c) sixth, and (d) tenth wave-packet revivals is depicted. Also shown are the results of the numerical model (line; see the Appendix) that successfully predicts the times of maximum net alignment as well as the chirp that centrifugal distortion introduces in the revival structure.

parameter $\langle\cos^2\vartheta\rangle$ yields information regarding the distribution of $|J\rangle$ states which comprise the rotational wave packet. The result is a spectrum of beat frequencies $\Delta\omega$ between states $|J\rangle$ and $|J+N\rangle$ whose magnitudes are proportional to the product of the quantum amplitudes $|a_J||a_{J+N}|$ (see the Appendix for details). Neglecting centrifugal distortion, the beat frequencies $\Delta\omega_{J,J+N}$ are given by

$$\Delta\omega_{J,J+N}=\frac{E_{J+N}}{\hbar}-\frac{E_J}{\hbar}=[2NJ+N^2+N]\frac{\omega_1}{2}. \qquad (4)$$

For a diatomic molecule, $\Delta J=0,2$, and the dominant beat frequencies are

$$\Delta\omega_{J,J+2}=(4J+6)\frac{\omega_1}{2}. \qquad (5)$$

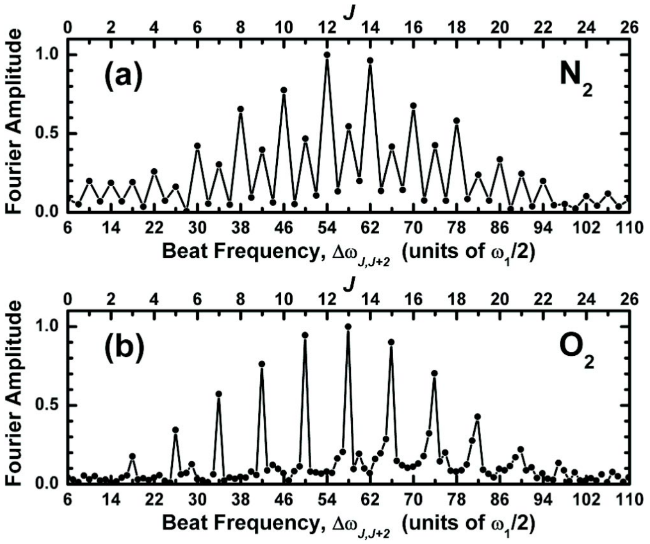

FIG. 6. Fourier transforms of (a) N_2 and (b) O_2 revival structures. Each spectrum represents the decomposition of a molecular revival structure into beat frequencies between constituent $|J\rangle$ states. In both cases, the observed beat frequencies are in accord with the prediction $\Delta\omega_{J,J+2}=(4J+6)(\omega_1/2)$. For O_2, only odd $|J\rangle$ states are populated. N_2, however, exists in both ortho (J even) and para (J odd) forms. The $\sim 2{:}1$ intensity alternation in (a) arises from the 2:1 relative abundance of ortho-N_2 versus para-N_2.

The time dependence of $\langle\cos^2\vartheta\rangle$ stems directly from the Fourier sum of such frequency components. The Fourier transform of the time variation of $\langle\cos^2\vartheta\rangle$ spanning one full period of the N_2 revival structure [i.e., 0–9 ps, Fig. 4(a)] is depicted in Fig. 6(a). The observed beat frequencies are in accord with the predictions of Eq. (5). The corresponding distribution of $|J\rangle$ states is approximately Gaussian, spans $J\sim 4$ to $J\sim 22$, and has a mean value of $J\sim 13$.

The nuclear spin statistics of N_2 are evident in the Fourier transform of its revival structure. Since ^{14}N has nuclear spin $I=1$, the molecule's total nuclear spin can take on the values $T=0$, 1, or 2 and N_2 exists in ortho ($T=0,2$; J even) and para ($T=1$; J odd) forms. Since a state with total nuclear spin T has degeneracy $2T+1$, the expected statistical weights of ortho-N_2 and para-N_2 are 6 (i.e., $1+5$) and 3, respectively. Hence, the relative abundance of ortho-N_2 versus para-N_2 is 2:1. This is reflected in the $\sim 2{:}1$ intensity alternation between spectral lines corresponding to J even and J odd in the Fourier transform [Fig. 6(a)]. Conversely, ^{16}O has nuclear spin $I=0$. Hence, O_2 exists in a single form for which only odd $|J\rangle$ states are populated. The Fourier transform of the alignment parameter $\langle\cos^2\vartheta\rangle$ for two full periods of the O_2 revival structure is depicted in Fig. 6(b). As expected, only spectral lines corresponding to odd $|J\rangle$ states appear, whose positions are given by Eq. (5).

The different nuclear spin statistics of N_2 and O_2 are also evident in their revival structures. At the first quarter revival (i.e., $t=T_0+\frac{1}{4}T_1$), the phase difference (modulo 2π) between states $|J\rangle$ and $|J+2\rangle$ is $\pi/2$. Near the quarter-revival time, the even $|J\rangle$ states form a secondary wave packet while the odd $|J\rangle$ states form another. The two secondary wave packets are oppositely localized. That is, when one second-

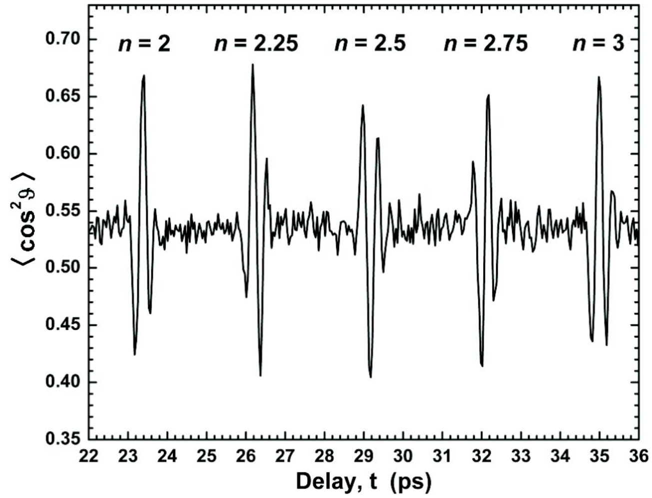

FIG. 7. $\langle \cos^2 \vartheta \rangle$ revival structure of O_2. The time variation of $\langle \cos^2 \vartheta \rangle$ is depicted, spanning the second and third full revivals as well as the 2.25, 2.5, and 2.75 fractional revivals. Since only odd $|J\rangle$ states are populated in O_2, the 2.25 and 2.75 revivals are not suppressed (as is the case in N_2; Fig. 4).

ary packet is principally distributed along the alignment axis, the other is localized primarily in the perpendicular plane. For a wave packet in which even and odd $|J\rangle$ states are equally populated, the opposite localizations would cancel at the time of the quarter revival and no net alignment (or antialignment) would be observed. In the case of N_2, both even and odd $|J\rangle$ states are populated but twice as much population exists in even states than in odd states. As a result, the temporary localization of the even secondary wave packet is only partially canceled by its odd counterpart. Thus, some net N_2 alignment and antialignment is observed near $t = T_0 + \frac{1}{4}T_1 = 2.163$ ps [Fig. 4(a)]. In the case of O_2, however, odd $|J\rangle$ states alone are populated. Since only a single localized wave packet exists at the time of a quarter revival, strong net alignment and antialignment is observed in the vicinity of the 2.25 and 2.75 revivals ($t = 26.293$ ps and $t = 32.059$ ps, respectively) for O_2 (Fig. 7).

We investigated the dependence of the N_2 revival structure on aligning pulse intensity in the vicinity of the first half revival (Fig. 8). The baseline value of $\langle \cos^2 \vartheta \rangle$ increases monotonically as the aligning pulse intensity is increased from 0.4×10^{14} W/cm^2 to 3.4×10^{14} W/cm^2, reflecting an increased degree of incoherent alignment. The revival structure amplitude increases up to an intensity of 2.0×10^{14} W/cm^2. This behavior is as expected since the aligning pulse intensity reflects the depth of the associated optical potential well. The higher the aligning intensity, the deeper the potential well, and the larger the range of trapped $|J\rangle$ states. As observed, the maximum degree of alignment increases with the number of rotational states present in the superposition. At aligning intensities greater than 2.0×10^{14} W/cm^2, significant ionization of the N_2 molecules occurs and consequently the revival structure amplitude decreases.

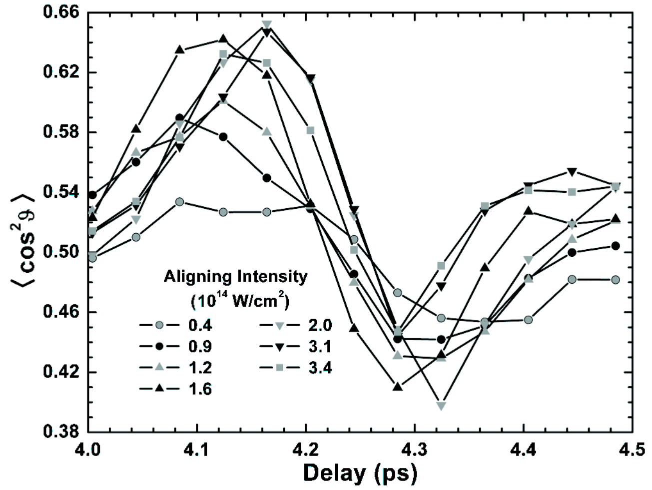

FIG. 8. Intensity variation of half revival for N_2. The time variation of $\langle \cos^2 \vartheta \rangle$ in the vicinity of the first half revival is depicted for several aligning pulse intensities. The baseline increases with aligning intensity. The amplitude of the revival structure increases for intensities up to 2.0×10^{14} W/cm^2. The transition from peak net alignment to maximum net antialignment becomes more rapid as the aligning intensity is increased.

As the aligning pulse intensity is increased, the alignment parameter $\langle \cos^2 \vartheta \rangle$ also varies more rapidly with time (Fig. 8). To better illustrate this effect, a single-cycle sinusoid was fitted to each revival structure shown in Fig. 8. The oscillation frequency ω_{osc} corresponding to each sinusoid increases monotonically over the intensity range for which little N_2 ionization occurs, i.e., 0.4×10^{14} W/cm^2 to 2.0×10^{14} W/cm^2 (Fig. 9). This trend can be understood in terms of the central $|J\rangle$ state of the rotational wave packet. According to Eq. (A6), the revival structure's dominant oscillation frequency ω_{osc} corresponds to the beat frequency $\Delta\omega_{J',J'+2}$ between

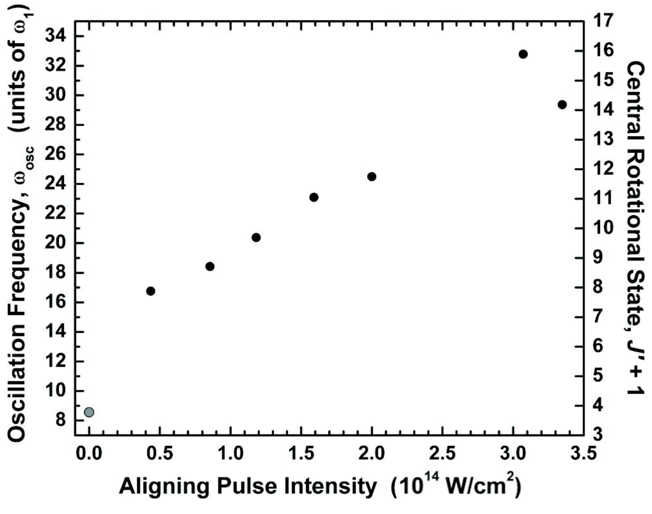

FIG. 9. Intensity variation of instantaneous frequency for N_2. The dominant oscillation frequencies ω_{osc}, of the measured N_2 revival structures (Fig. 8) as a function of aligning pulse intensity are shown (black circles). The central rotational states $|J+1\rangle$ of the corresponding wave packets are shown on the right axis. The increase in the central rotational state corresponds to a deepening of the optical potential well with aligning intensity. For comparison, the most populated rotational state of the 105 K molecular beam is plotted at zero intensity (gray circle).

the wave packet's two most highly populated $|J\rangle$ states J' and $J'+2$. Hence, the central rotational state of the wave packet (i.e., $J'+1$) can be determined from the measured value of ω_{osc} using Eq. (5). As shown in Fig. 9, the central rotational state is also observed to increase with aligning intensity. This is as expected since increasing the aligning intensity produces a deeper optical potential well and an increased value of $J'+1$.

V. TIME-DEPENDENT ANGULAR DISTRIBUTIONS

We observe a molecule's rotational dynamics by directly imaging molecular ϑ distributions at various moments during the time evolution of its rotational wave packet. While conventional revival structures (i.e., plots of $\langle\cos^2\vartheta\rangle$ vs time) such as Fig. 4(a) reflect net wave packet behavior, our time-dependent ϑ distributions yield considerably more insight regarding the actual distributions of molecular orientations.

To illustrate the utility of our imaging technique, measured ϑ distributions corresponding to significant points in the revival structure of N_2 [Fig. 4(a)] are presented. The molecular alignment axis lies along $\vartheta=0°$ and $\vartheta=180°$ and is therefore horizontal in our ϑ-distribution plots [Figs. 4(b)–4(d)]. During the first full wave packet revival ($t=8.462$ ps), the wave packet exhibits significant net alignment. This is reflected by measured (dots) and simulated (line) angular distributions [Fig. 4(d)] that are strongly peaked about the alignment axis and a corresponding peak value of $\langle\cos^2\vartheta\rangle$ in the revival structure [Fig. 4(a)]. The simulated angular distribution was obtained using the approach described in the Appendix followed by a projection of the entire wave packet onto the plane of polarization of the exploding pulse. At the half-revival time ($t=4.271$ ps), molecules lie predominantly in the plane perpendicular to the alignment axis. As a result, the corresponding ϑ distributions [Fig. 4(c)] are concentrated primarily along $\vartheta=90°$ and $\vartheta=270°$ and $\langle\cos^2\vartheta\rangle$ attains its minimum value. At $t=4.137$ ps, the wave packet exhibits significant net alignment [Fig. 4(b)] just prior to the first half revival which gives

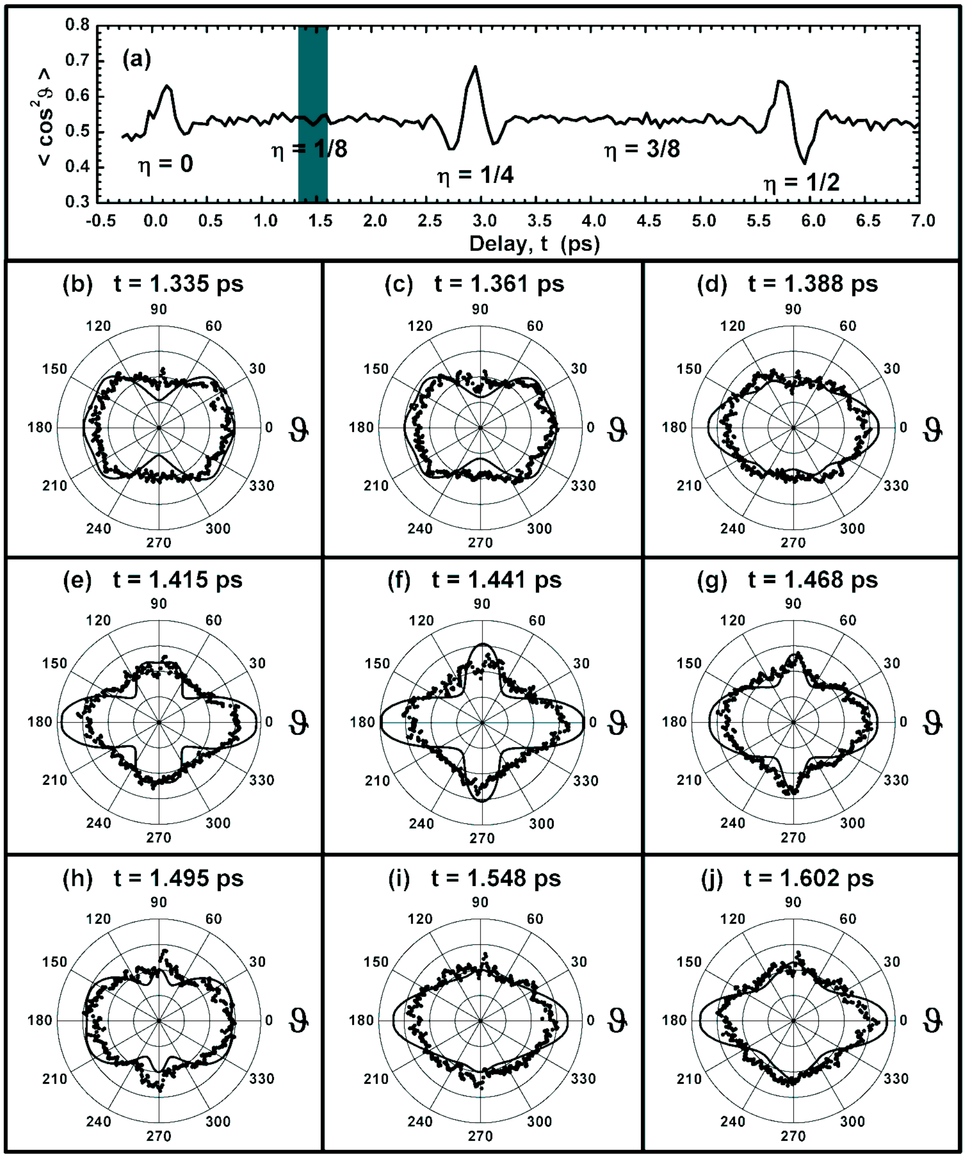

FIG. 10. (a) Revival structure of O_2. Locations of the ηth revivals are shown. The 1/8 revival occurs in the shaded region. (b)–(j) Plots of O_2 ϑ distributions near the 1/8 revival. The measured distributions (dots) follow the evolution of the model results (lines). Each measured distribution contains the results of 25 000 determinations of molecular orientation.

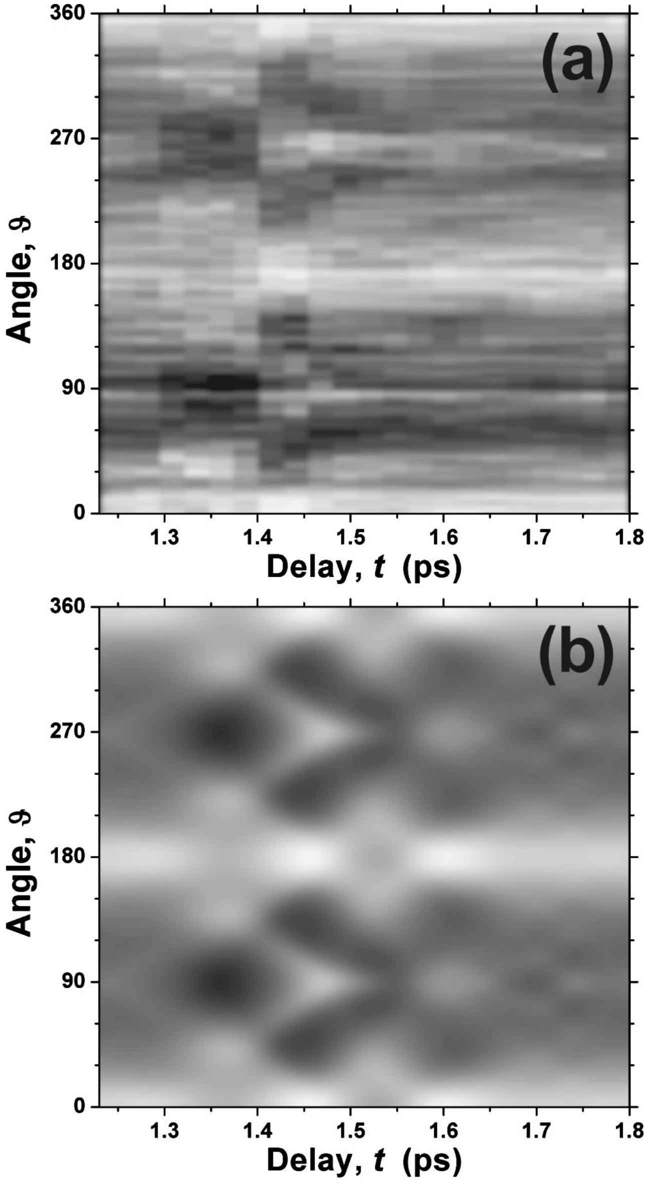

FIG. 11. Intensity maps of (a) measured and (b) simulated O_2 ϑ distributions near the 1/8 revival. The ϑ distribution (in degrees) at each time delay is plotted and labeled by shades of gray. Low probability density is represented by black, high density by white. Although grainy (due to the 27 fs experimental time increment), the measured intensity map captures the essence of the molecular dynamics.

rise to a peak value of $\langle\cos^2\vartheta\rangle$.

Since they reflect net wave packet behavior, $\langle\cos^2\vartheta\rangle$ revival structures [such as Figs. 4(a), 5, and 7] are useful for identifying times that correspond to significant net alignment or antialignment. Instances of net behavior are rare during the evolution of a rotational wave packet, however. Hence, $\langle\cos^2\vartheta\rangle$ revival structures consist of a relatively flat baseline punctuated by regions of peaks and troughs. While such baselines indicate a wave packet's degree of time-independent incoherent alignment, they provide no insight regarding molecular angular distributions at such times. Although minimal net alignment is observed in such baseline regions, the corresponding angular distributions can differ considerably. For instance, ϑ distributions for the isotropic case [analogous to a circle (○) in Figs. 4(b)–4(d)], a plus (+), a cross (×), and an asterisk (*) would each yield a net alignment parameter of $\langle\cos^2\vartheta\rangle=0.5$. To distinguish such qualitatively different distributions, an angle-resolved imaging technique is required.

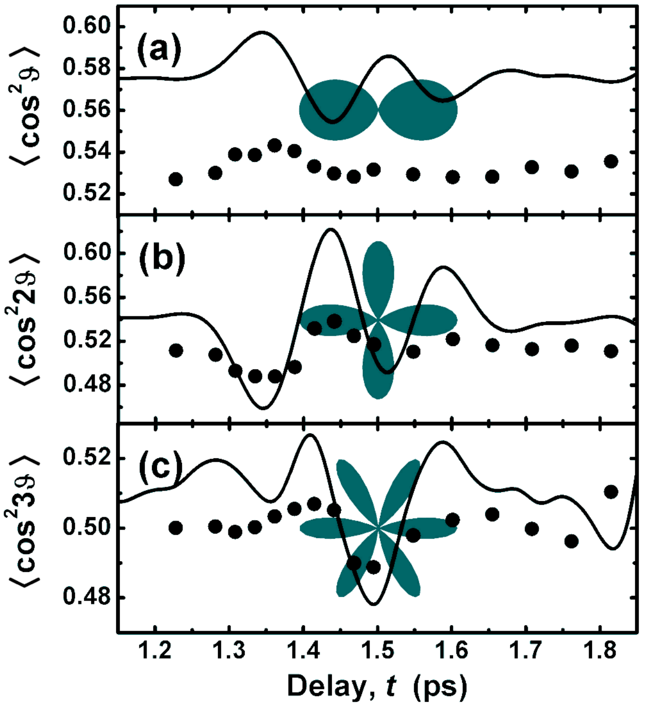

FIG. 12. Projections of O_2 ϑ distributions onto angular basis states. Time-dependent projections of the measured (dots) and simulated (line) ϑ distributions onto the (a) $\cos^2\vartheta$, (b) $\cos^2 2\vartheta$, and (c) $\cos^2 3\vartheta$ basis states are depicted in the vicinity of the 1/8 revival of O_2. Polar representations of the basis states are superimposed in gray.

Since we measure a molecular angular distribution at each time delay, we can follow a wave packet's evolution even during periods of minimal net alignment. As an illustration, we present the results of imaging performed in the vicinity of the 1/8 revival in O_2 ($t\sim1.4$ ps). The 1/8 revival occurs in the baseline region of the $\langle\cos^2\vartheta\rangle$ revival structure of O_2 [Fig. 10(a)]. Figures 10(b)–10(j) depict both measured (dots) and simulated (lines) ϑ distributions in the vicinity of the 1/8 revival. The value of $\langle\cos^2\vartheta\rangle$ is approximately equal for each distribution and the time increment for most of those shown is just 27 fs. Nevertheless, we can qualitatively resolve such structures as a bowtie [Fig. 10(c)], a plus [Fig. 10(f)], and a butterfly [Fig. 10(h)].

Our time-dependent angular distributions can be compactly represented using the scheme of Fig. 11. Intensity maps for the measured [Fig. 11(a)] and simulated [Fig. 11(b)] angular distributions in the vicinity of the 1/8 revival of O_2 are depicted. White, gray, and black represent regions of high, intermediate, and low probability density, respectively. Although the 27 fs temporal resolution introduces a noticeable graininess, the measured intensity map captures the essential features of the molecular dynamics. Incoherent alignment is manifested by light streaks along the alignment axis (i.e., $\vartheta = 0°$, 180°, and 360°). Dark regions centered at $\vartheta = 90°$ and $\vartheta = 270°$ reflect the appearance of the bowtie distribution [Fig. 10(c)] at $t = 1.361$ ps. The plus distribution [Fig. 10(f)] appears at $t = 1.441$ ps as four bright centers (at $\vartheta = 0°$, 90°, 180°, 270°, and 360°) with two intervening diamond-shaped dark regions. A lower contrast replica of the plus distribution occurs at $t = 1.602$ ps [Fig. 10(j)]. As a result, the corresponding centers and diamonds are less distinct in the intensity maps.

We can also represent our measured ϑ distributions $S(\vartheta,t)$ by projecting them onto an angular basis set of our choosing. For example, we can expand the angular data in terms of squared cosines, i.e., $S(\vartheta,t) = \Sigma_{n=0}^{\infty} c_n(t)\cos^2(n\vartheta)$. Note that the $n=1$ term of this expansion corresponds to the $\langle \cos^2 \vartheta \rangle$ revival structure used throughout this work to characterize the degree of wave-packet alignment along the aligning pulse polarization [e.g., Fig. 10(a)]. Since we measure $S(\vartheta,t)$, however, we can also compute higher-order $\langle \cos^2(n\vartheta) \rangle$ revival structures corresponding to other terms of the expansion. To illustrate this, projections of the measured (dots) and simulated (lines) O_2 angular distributions in the vicinity of the 1/8 revival onto the $n = 1,2,3$ states of the $\cos^2(n\vartheta)$ basis are shown in Fig. 12.

Of practical interest is our ability to efficiently search for an arbitrary target angular distribution $F(\vartheta)$ using our technique, even during data acquisition. This can be achieved in the laboratory by monitoring the generalized revival structure

$$G(t) = \frac{\int S(\vartheta,t)F(\vartheta)d\vartheta}{\int S(\vartheta,t)d\vartheta \int F(\vartheta)d\vartheta}. \tag{6}$$

Peaks in $G(t)$ denote times at which the measured angular distribution best corresponds to the target distribution, just as peaks in a $\langle \cos^2 \vartheta \rangle$ revival structure indicate times of maximum net molecular alignment.

VI. CONCLUSIONS AND PERSPECTIVES

Using molecular Coulomb explosion as a probe, we directly image rotational wave packets and obtain $\langle \cos^2 \vartheta \rangle$ revival structures for N_2 and O_2 with up to 27 fs time resolution. We have presented angular distributions corresponding to net field-free molecular alignment of N_2 during a full rotational wave-packet revival as well as net antialignment during a half revival. Further, we have presented a series of angular distributions that reflect the rich dynamical behavior near the eighth-revival in O_2 for which no significant alignment occurs.

The ability to produce field-free ensembles of aligned molecules has enabled us to measure the directional dependence of the multiphoton ionization rate of N_2 [15]. In the future, the ability to minimize orientational averaging should simplify experiments involving ultrafast electron diffraction [24], electron self-diffraction [16], and photoelectron angular distributions [25].

To perform rotational imaging, we measured the three-dimensional velocity vector of a single ion fragment per molecule. However, we can also measure and correlate the three-dimensional velocities of multiple ion fragments. Technically, this permits optically triggered Coulomb explosion imaging [26] of the internal dynamics of small and intermediate polyatomic molecules.

APPENDIX: CALCULATION OF WAVE-PACKET DYNAMICS

The calculation of the aligning pulse-molecule interaction and the resulting field-free rotational revivals was performed as follows. The aligning pulse interacts with the molecular wave function through the nonresonant ac Stark shift [5]

$$i\Psi(\theta,t) = [B\mathbf{J}^2 - U(t)\cos^2(\theta)]\Psi(\theta,t), \tag{A1}$$

where θ is the angle between the laser polarization and the molecular axis, $\mathbf{J}$ is the angular momentum operator, B is the rotational constant of the molecule in question, and

$$U(t) = \frac{1}{4}(\alpha_{\parallel} - \alpha_{\perp})\mathcal{E}^2(t). \tag{A2}$$

Here $\alpha_{\parallel}$ and $\alpha_{\perp}$ are the polarizability components parallel and perpendicular to the molecular axis and $\mathcal{E}(t)$ is the electric field strength. The pulse shapes considered have the form

$$\mathcal{E}^2(t) = \mathcal{E}_0^2 \sin^2\left(\frac{\pi t}{2\tau_{\mathrm{on}}}\right), \tag{A3}$$

where $\mathcal{E}_0$ is the electric field amplitude and τ_{on} gives the time for the pulse to rise from zero to peak amplitude (and is also the full width at half maximum of the pulse). The evolution of the wave function over the duration of the aligning pulse was calculated numerically using a Crank-Nicholson scheme [27] in $|J,M\rangle$ space.

With the rotational superposition at the end of the pulse written as

$$\Psi_0 = \sum_J a_J |J,M\rangle, \tag{A4}$$

the field-free evolution of the wave packet becomes

$$\Psi(t) = \sum_J a_J e^{-i(E_J/\hbar)t} |J,M\rangle, \tag{A5}$$

where $E_J = B_0 J(J+1) - D_e[J(J+1)]^2$. Note that cylindrical symmetry of the potential well prevents the coupling of different M values. The time-dependent measure of alignment is given by

$$\langle \cos^2\theta\rangle = \langle \Psi(t)|\cos^2\theta|\Psi(t)\rangle = \sum_J |a_J|^2 C_{J,J,M} + |a_J||a_{J+2}| \times \cos(\Delta\omega_{J,J+2}t + \varphi_{J,J+2}) C_{J,J+2,M}, \tag{A6}$$

where

$$C_{J,J,M} = \langle J,M|\cos^2\theta|J,M\rangle,$$

$$C_{J,J+2,M} = \langle J,M|\cos^2\theta|J+2,M\rangle, \tag{A7}$$

$$\Delta\omega_{J,J+2} = \frac{E_{J+2}}{\hbar} - \frac{E_J}{\hbar},$$

and $\varphi_{J,J+2}$ denotes the relative phase between the states $|J,M\rangle$ and $|J+2,M\rangle$ at the start of the field-free evolution. The alignment signal was further averaged over an initial distribution of angular states at a given temperature T.

Centrifugal distortion was included by writing the $B\mathbf{J}^2$ operator as $B_0 J(J+1) - D_e[J(J+1)]^2$ in $|J,M\rangle$ space [22] with $B_0 = 1.989\,581\ \mathrm{cm}^{-1}$ and $D_e = 5.76\times 10^{-6}\ \mathrm{cm}^{-1}$ for N_2 and $B_0 = 1.4297\ \mathrm{cm}^{-1}$ and $D_e = 4.839\times 10^{-6}\ \mathrm{cm}^{-1}$ for O_2 [23]. Further corrections to the kinetic energy arising from vibrational excitation can be neglected since fewer than one in 10^5 N_2 or O_2 molecules are vibrationally excited at temperatures below 300 K [22].

The initial rotational temperature T, the electric field amplitude $\mathcal{E}_0$, and the duration of the pulse τ_{on} were varied until the calculated revival structure best matched the measured revivals. The comparison was done using the Fourier transform of the alignment signal [Eq. (A1)] which readily yields the distribution of populated $|J,M\rangle$ states through the amplitude terms $|a_J||a_{J+2}|$ labeled by the corresponding beat frequencies $\Delta\omega_{J,J+2} \approx B_0(4J+6)$. The best agreement resulted for an initial rotational temperature of $T = 105$ K and aligning pulse parameters of $\tau_{\mathrm{on}} = 48.4$ fs and $\mathcal{E}_0{}^2 = 1.7\times 10^{14}$ W/cm^2.

The calculation captures many features of the revival structure well. The times of maximum net alignment as well as the chirp of the revival structure are well reproduced. The calculated and experimental magnitudes of the baseline and the signal oscillations differ, however. Some (if not all) of this discrepancy is due to aperture effects of the exploding pulse that have not been fully incorporated into the model calculation.

---

[1] P.B. Corkum, Ch. Ellert, M. Mehendale, P. Dietrich, S. Hankin, S. Aseyev, D. Rayner, and D. Villeneuve, Faraday Discuss. **113**, 47 (1999).

[2] T. Takekoshi, B.M. Patterson, and R.J. Knize, Phys. Rev. Lett. **81**, 5105 (1998).

[3] H. Stapelfeldt, Hirofumi Sakai, E. Constant, and P.B. Corkum, Phys. Rev. Lett. **79**, 2787 (1997).

[4] J. Karczmarek, J. Wright, P. Corkum, and M. Ivanov, Phys. Rev. Lett. **82**, 3420 (1999); D.M. Villeneuve, S.A. Aseyev, P. Dietrich, M. Spanner, M.Yu. Ivanov, and P.B. Corkum, *ibid.* **85**, 542 (2000); M. Spanner and M.Yu. Ivanov, J. Chem. Phys. **114**, 3456 (2001); M. Spanner, K.M. Davitt, and M.Yu. Ivanov, *ibid.* **115**, 8403 (2001).

[5] B. Friedrich and D. Herschbach, Phys. Rev. Lett. **74**, 4623 (1995).

[6] T. Seideman, J. Chem. Phys. **103**, 7887 (1995).

[7] W. Kim and P.M. Felker, J. Chem. Phys. **104**, 1147 (1996).

[8] H. Sakai, C.P. Safvan, J.J. Larsen, K.M. Hilligsøe, K. Hald, and H. Stapelfeldt, J. Chem. Phys. **110**, 10 235 (1999); J.J. Larsen, H. Sakai, C.P. Safvan, I. Wendt-Larsen, and H. Stapelfeldt, *ibid.* **111**, 7774 (1999); J.J. Larsen, K. Hald, N. Bjerre, H. Stapelfeldt, and T. Seideman, Phys. Rev. Lett. **85**, 2470 (2000).

[9] B. Friedrich, D.P. Pullman, and D.R. Herschbach, J. Phys. Chem. **95**, 8118 (1991).

[10] V.A. Cho and R.B. Berstein, J. Phys. Chem. **95**, 8129 (1991).

[11] T. Seideman, Phys. Rev. A **56**, R17 (1997).

[12] J. Ortigoso, M. Rodríguez, M. Gupta, and B. Friedrich, J. Chem. Phys. **110**, 3870 (1999); T. Seideman, Phys. Rev. Lett. **83**, 4971 (1999).

[13] F. Rosca-Pruna and M.J.J. Vrakking, Phys. Rev. Lett. **87**, 153902 (2001); F. Rosca-Pruna and M.J.J. Vrakking, J. Chem. Phys. **116**, 6567 (2002); **116**, 6579 (2002).

[14] V. Kalosha, M. Spanner, J. Herrmann, and M.Yu. Ivanov, Phys. Rev. Lett. **88**, 103901 (2002); D.M. Villeneuve, S.A. Aseyev, A. Avery, and P.B. Corkum, Appl. Phys. B: Lasers Opt. **74**, S157 (2002); J. Underwood, M. Spanner, M.Yu. Ivanov, J. Mottershead, B.J. Sussman, and A. Stolow, Phys. Rev. Lett. **90**, 223001 (2003).

[15] I.V. Litvinyuk, K.F. Lee, P.W. Dooley, D.M. Rayner, D.M. Villeneuve, and P.B. Corkum, Phys. Rev. Lett. **90**, 233003 (2003).

[16] H. Niikura, F. Légaré, R. Hasbani, A.D. Bandrauk, M.Yu. Ivanov, D.M. Villeneuve, and P.B. Corkum, Nature (London) **417**, 917 (2002).

[17] L.J. Frasinski, K. Codling, P. Hatherly, J. Barr, I.N. Ross, and W.T. Toner, Phys. Rev. Lett. **58**, 2424 (1987); T. Zuo, S. Chelkowski, and A.D. Bandrauk, Phys. Rev. A **48**, 3837 (1993); T. Seideman, M.Yu. Ivanov, and P.B. Corkum, Phys. Rev. Lett. **75**, 2819 (1995); E. Constant, H. Stapelfeldt, and P.B. Corkum, *ibid.* **76**, 4140 (1996).

[18] Ch. Ellert and P.B. Corkum, Phys. Rev. A **59**, R3170 (1999).

[19] C. Iaconis and I.A. Walmsley, Opt. Lett. **23**, 792 (1998).

[20] S.E. Sobottka and M.B. Williams, IEEE Trans. Nucl. Sci. **35**, 348 (1988); O. Jagutzki, V. Mergel, K. Ullmann-Pfleger, L. Spielberger, U. Meyer, R. Dörner, and H. Schmidt-Böcking, Proc. SPIE **3438**, 322 (1998).

[21] L.J. Frasinski, K. Codling, and P.A. Hatherly, Science **246**, 1029 (1989).

[22] G. Herzberg, *Molecular Spectra and Molecular Structure: Volume I—Spectra Of Diatomic Molecules*, 2nd ed. (Krieger, Malabar, FL, 1989).

[23] K.P. Huber and G. Herzberg (data prepared by J.W. Gallagher and R.D. Johnson III), in "NIST Chemistry WebBook," NIST Standard Reference Database Number 69, edited by P.J. Lin-

strom and W.G. Mallard, National Institute of Standards and Technology, Gaithersburg, MD, 2001 (http://webbook.nist.gov).

[24] J.C. Williamson, J. Cao, H. Ihee, H. Frey, and A.H. Zewail, Nature (London) **386**, 159 (1997).

[25] O. Geßner, Y. Hikosaka, B. Zimmerman, A. Hempelmann, R.R. Lucchese, J.H.D. Eland, P.-M. Guyon, and U. Becker, Phys. Rev. Lett. **88**, 193002 (2002).

[26] Z. Vager, R. Naaman, and E.P. Kanter, Science **244**, 426 (1989); P.W. Dooley, V.R. Bhardwaj, and P.B. Corkum, in *Proceedings of the International Conference on Lasers '99* (STS Press, McLean, VA, 2000), p. 8.

[27] W.H. Press *et al.*, *Numerical Recipes*, 2nd ed. (Cambridge University Press, Cambridge, England, 1992).